



Numerical Investigation of Second-Mode Attenuation over Carbon/Carbon Porous Surfaces

Victor C. B. Sousa,* Danish Patel,† and J.-B. Chapelier‡
Purdue University, West Lafayette, Indiana 47906
 Viola Wartemann§ and Alexander Wagner¶
DLR, German Aerospace Center, Göttingen, Germany
 and
 Carlo Scalo**
Purdue University, West Lafayette, Indiana 47906

DOI: 10.2514/1.A34294

Axisymmetric direct numerical simulations of a spatially developing hypersonic boundary layer over a sharp 7 deg half-angle cone at $M_\infty = 7.5$ at Reynolds numbers $Re_m = 1.46 \cdot 10^6, 2.43 \cdot 10^6,$ and $4.06 \cdot 10^6 \text{ m}^{-1}$ have been carried out. The streamwise extent of the simulated domain is 0.9 m. The boundary layer is excited with the one-time application of a broadband pulse that is advected downstream over an impermeable wall and a complex impedance boundary condition (IBC) modeling the acoustic response of carbon/carbon (C/C) ultrasonically absorptive porous surfaces. The complex IBCs are derived as an output of a pore-scale aeroacoustic analysis: the inverse Helmholtz solver (IHS) and algebraic low-order models. The IHS estimate of the C/C impedance is compared to other methods for porous acoustic absorbers, revealing uncertainties in the applicability of analytical models for porous absorbers. The introduction of the IBCs in all cases leads to a significant attenuation of the instability waves, up to one order of magnitude reduction in pressure perturbation amplitude for the $Re_m = 4.06 \cdot 10^6 \text{ m}^{-1}$ case.

Nomenclature

a	=	speed of sound, m/s
C/C	=	carbon/carbon
f	=	frequency, kHz
H	=	depth, m
\Im	=	imaginary
L	=	distance from the leading edge, m
M	=	Mach number
Pr	=	Prandtl number
p	=	pressure, Pa
p_k	=	poles
\hat{R}	=	complex reflection coefficient
\Re	=	real
Re	=	Reynolds number
\hat{S}	=	complex absorption coefficient
T	=	temperature, K
u or U	=	streamwise velocity, m/s
x	=	streamwise direction, m
y	=	wall-normal direction, m
Z	=	impedance, (Pa · s)/m
β	=	absorption coefficient

γ	=	ratio of specific heats
θ	=	angle of incidence
κ	=	structure factor
λ	=	wavelength, m
μ_k	=	residues
Ξ	=	resistivity, (MPa · s)/m ²
ρ	=	density, kg/m ³
ϕ	=	porosity
ψ	=	zenith angle in spherical coordinate system
ω	=	frequency, rad/s

Subscripts

c	=	cone
e	=	boundary-layer edge
w	=	wall
∞	=	freestream
*	=	nondimensional
0	=	base state

I. Introduction

THE design of hypersonic vehicles is constrained by the considerable heat transfer and shear-stress loads imparted on the vehicles surface by the boundary layer. While being already critical in the laminar regime, such loads are significantly enhanced by the transition to turbulence. Reed et al. [1] highlighted the differences in fully turbulent and fully laminar trajectories for a hypersonic flight vehicle, reporting that the vehicle would experience a heat flux approximately five times higher under turbulent conditions and therefore would require at least twice the weight in thermal protection systems (TPS). Recent studies in the framework of the national Aerospace Plane Project led by the Defense Science Board committee [2] quantify the drop in performance of high-speed vehicles due to transition, reporting that the payload-to-weight ratio for fully laminar conditions is three times larger than for fully turbulent. These studies emphasize the importance of laminar-to-turbulent transition delay for sustainability of high-speed flight and the need for any realizable technology for boundary-layer control to be symbiotic with TPS.

Hypersonic vehicles that fly at small angles of attack and with high lift-to-drag ratios tend to have predominantly symmetric geometries

Presented as Paper 2018-0350 at the 2018 AIAA Aerospace Sciences Meeting, Kissimmee, FL, 8–12 January 2018; received 4 May 2018; revision received 20 August 2018; accepted for publication 21 August 2018; published online 16 November 2018. Copyright © 2018 by the American Institute of Aeronautics and Astronautics, Inc. All rights reserved. All requests for copying and permission to reprint should be submitted to CCC at www.copyright.com; employ the ISSN 0022-4650 (print) or 1533-6794 (online) to initiate your request. See also AIAA Rights and Permissions www.aiaa.org/randp.

*Graduate Research Assistant, School of Mechanical Engineering; vsousa@purdue.edu. Student Member AIAA.

†Graduate Research Assistant, School of Mechanical Engineering; patel472@purdue.edu. Student Member AIAA.

‡Postdoctoral Fellow, School of Mechanical Engineering; jchapeli@purdue.edu. Fellow Member AIAA.

§Research Scientist, Spacecraft Department, Institute of Aerodynamics and Flow Technology; viola.wartemann@dlr.de.

¶Research Scientist, Spacecraft Department, Institute of Aerodynamics and Flow Technology; Alexander.Wagner@dlr.de.

**Assistant Professor, School of Mechanical Engineering; scalo@purdue.edu. Member AIAA.

and slender shapes. Under these conditions, second-mode waves become the main mechanism driving transition to turbulence [3]. The second mode was discovered by Mack [4] and consists of traveling ultrasonic acoustic waves trapped within the boundary layer; they are found to be amplified by wall-cooling conditions, that is when the wall temperature is below adiabatic temperatures, $T_w < T_{ad}$, which is commonly the case. Mack's studies on the evolution of these and higher modes [5] stressed the importance of second-mode attenuation in any attempt to increase the transitional Reynolds number in high-speed flows.

Malmuth et al. [6] proved through linear stability theory (LST) the capability of ultrasonically absorbing coatings (UACs) to mitigate the second mode, confirmed by experiments that followed. The first experimental validation of this principle is due to Fedorov et al. [7], who constructed a cone with a half-angle of 5 deg with two different surfaces: one smooth and impermeable, and the other perforated with regularly spaced micro holes. They reported that the porous surface was capable of doubling the transitional Reynolds number in comparison with the smooth surface in experiments at Mach 5 at the T-5 hypersonic wind tunnel located at the California Institute of Technology.

The development of UACs continued, with the goal of combining the acoustic absorption and TPS characteristics into one solution. Knowing that an irregular porous structure is naturally found in TPS materials used for hypersonic vehicles, Fedorov et al. [8,9] conducted experiments in the Mach 6 wind tunnel T-326 at the Institute of Theoretical and Applied Mechanics (ITAM) in Novosibirsk, Russia, over a felt-metal surface with an irregular porous structure (as well as another surface with regular microstructure). These experiments were the first to produce data capable of quantitatively demonstrating the attenuation of the second-mode waves via UACs, confirmed by stability analysis, but also showed a small destabilization of the first mode.

Chokani et al. [10] performed a bispectral analysis on this same data with the goal of identifying nonlinear mechanisms that could be triggered by the use of porous coatings; this was motivated by the observation of a weak enhancement of first-mode waves. The experiments revealed the occurrence of nonlinear phase locking, which is the most efficient method for a mode to feed itself or to transfer energy between modes, involving only the first mode, in the presence of porous walls and not over an impermeable surface. This effect was also shown to be small, not impacting the overall stabilizing role of the porous coating. More recently, Lukashovich et al. [11], performed new experiments in ITAM's tunnel, where it was shown that placing the porous insert in the region where the second mode is stable leads to an increase in the disturbance signal amplitude; the opposite is observed when the insert is placed in regions of second-mode growth.

Inspired by some of these results, Wagner et al. [12–14] pioneered the use of carbon/carbon (C/C), an intermediate state of C/C silicon carbide (C/C-SiC) already employed on hypersonic vehicles [15,16], to control second-mode waves. Experiments at Mach 7.5 have been conducted in the DLR High Enthalpy Shock Tunnel Göttingen (HEG), and the stabilization of the second mode as well as an increase in the laminar portion of the boundary layer over the porous surface have been observed. For these flow conditions, Wartemann et al. [17] have performed an analysis based on the parabolized stability equations, confirming the effectiveness of porous surfaces based on C/C in achieving transition delay. The present paper is the first step toward performing a full direct numerical simulation of a spatially developing boundary layer over a conical surface with assigned complex broadband wall-impedance representative of the distributed random porosity of C/C surfaces.

Most of previous high-fidelity numerical studies of attenuating, canceling, or reinforcing second-mode instabilities in high-speed flow

over porous walls have focused on uniformly spaced and/or geometrically regular porosity in temporally developing boundary layers [18–22]. More recently, Wang and Zhong [23] have performed direct numerical simulations of a hypersonic boundary layer over a flat plate modeling the effects of the irregular felt-metal surface used in the experiments conducted by Fedorov et al. [9]. Their studies concluded that the modeled felt-metal porous surface destabilized the first mode and attenuated the second, consistent with the experiments.

The current paper will focus on axisymmetric flow over a sharp 7 deg half-angle cone, analyzing the three lowest Reynolds numbers investigated in the experiments by Wagner et al. [12,13] (see Table 1). The novelty of the adopted computational approach lies in the time-domain impedance boundary conditions (TDIBC) technique, as implemented by Scalo et al. [24] in the context of subsonic compressible near-wall turbulence, allowing the exact application of any complex impedance boundary conditions in direct numerical simulations.

II. Physical Model and Computational Approach

The numerical study performed in this work is based on tests conducted by Wagner [13] in the DLR High Enthalpy Shock Tunnel Göttingen (HEG). In the present study, test conditions of $Re_m = 1.46 \cdot 10^6 \text{ m}^{-1}$, $Re_m = 2.43 \cdot 10^6 \text{ m}^{-1}$, and $Re_m = 4.06 \cdot 10^6 \text{ m}^{-1}$ are chosen; all freestream conditions and the parameters of these runs are reported in Table 1. Simulations of spatially developing boundary layer are carried out over a 0.95-m-length cone, starting at 0.05 m from the tip. A sharp cone with a half-angle of 7 deg is the geometry of choice, being an idealization of Wagner's 2.5 mm round-tip cone model actually employed for the transition delay experiments over C/C.

High-order structured compact-finite-difference simulations are carried out with the CFDSU solver (more details are given in Sec. III.A) with the objective of capturing the perturbation evolution with minimum numerical dissipation and high resolving power for a given amount of points per wavelength. Simulations are performed with inlet flow conditions to the high-order simulations starting at $x = 0.05 \text{ m}$ from the tip (Fig. 1) and informed by combining the Taylor–Maccoll [25] inviscid solution with a viscous solution for the boundary layer. The latter is derived by applying the Mangler [26] transformation for bodies of rotation to the compressible boundary-layer similarity solution for a perfect gas over a flat plate [27], as done by Lees [28] for the flow over a cone.

Using this transformation, one can describe the spatial evolution of a boundary layer through the use of the following similarity variables:

$$\xi = \int_0^x \rho_e U_e \mu_e r_{\perp}^2 dx \quad (1)$$

$$\eta = \frac{U_e r_{\perp}}{\sqrt{2\xi}} \int_0^y \rho dy \quad (2)$$

where x is the streamwise direction (tangential to the wall), y the direction normal to the wall, and $r_{\perp}(x)$ is the cone radius as measured perpendicularly to its axis of rotational symmetry.

Noting that, for a cone of half-angle ψ_c , the radius of cross section of a body of revolution can be written as $r_{\perp} = x \sin \psi_c$ and that the flow properties after a conical shock are constant along straight lines originating from the tip of the cone, it is assumed that the properties at the boundary-layer edge are independent of x , and hence the similarity variables 1 and 2 can be simplified to

Table 1 Selected flow parameters from Wagner's experiments [13]

Re_m, m^{-1}	M_{∞}	p_{∞}, Pa	T_{∞}, K	$\rho_{\infty}, \text{kg/m}^3$	$u_{\infty}, \text{m/s}$	p_e, Pa	T_e, K	$\rho_e, \text{kg/m}^3$	$u_e, \text{m/s}$
1.46×10^6	7.3	789	267	0.0102	2409	1944	345	0.0187	2376
2.43×10^6	7.4	1453	285	0.0177	2480	3443	368	0.0324	2446
4.06×10^6	7.4	2129	268	0.0276	2422	5076	347	0.0508	2388

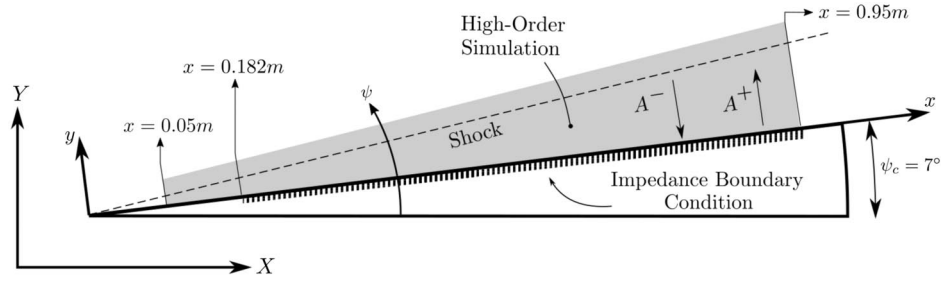


Fig. 1 Computational setup of DNS of second-mode waves over complex impedance boundary conditions.

$$\xi = \frac{\rho_e U_e \mu_e x^3 \sin^2 \psi}{3} \tag{3}$$

$$\eta = \sqrt{\frac{3U_e}{2x\rho_e\mu_e}} \int_0^y \rho dy \tag{4}$$

This allows to numerically solve the boundary-layer equations as a nonlinear ordinary differential equation (ODE) with η as the only dimensionless coordinate over which to perform the integration. In practice, the solution is generated on a very fine grid in the η space and then mapped back to the (x, y) space and interpolated bilinearly on the grid used to perform the Navier–Stokes calculations. As shown in Fig. 2, excellent matching is observed between the thus-obtained semi-analytical flow and steady Navier–Stokes calculations.

Simulations are first carried out under quiet conditions (no perturbations), allowing the mean flow to be fully established and all residual perturbations (artifacts of the flow initialization, retained by the low-dissipation numerics) to be convected out of the domain. The solution was allowed to relax on the Navier–Stokes grid for approximately four flow-through cycles, based on the freestream velocity and the domain extent, before perturbations were applied.

The grid used to discretize the conical domain is a structured spherical grid with the origin at the tip of the cone. The version of CFDSU under development at Purdue University is able to perform a trivariate coordinate system transformation, mapping a general curvilinear coordinate system onto a uniform and orthogonal spatial domain. The choice of spherical coordinates guarantees perfect orthogonality (reduced numerical errors in the grid transformation step) between gridlines and is advantageous because it can be described very trivially analytically. The disadvantage of this grid is that the resolution in the wall-normal direction (y) decreases as we move away from the origin; this issue is mitigated by the streamwise

boundary-layer growth. The spherical grid is stretched in the wall-normal (angular) direction with a half-tangent hyperbolic law to resolve not only the boundary layer of the mean flow but also the acoustic-wave-induced Stokes boundary-layer thickness.

The inflow plane of the high-order Navier–Stokes simulations is located under the shock, at a streamwise distance of $x = 0.05$ m from the tip (Fig. 1). Here, hardly imposed Dirichlet boundary conditions are used, informed from the precalculated semi-analytical steady laminar viscous solution described previously. Outlet conditions are homogeneous Neumann for all flow quantities. At the wall, no-slip, no-penetration and (when and where active) suction and blowing conditions are imposed. At the top boundary (above the shock), steady freestream conditions are imposed.

Inlet and outlet sponge layers of approximately 0.045 m in thickness are used to control spurious oscillations due to the introduction of the shock in the domain at the inlet and to prevent the formation of upstream traveling disturbances near the outlet, in both cases arising in the subsonic portion of the boundary layer. These layers relax the instantaneous flow to the aforementioned semi-analytical steady laminar solution.

A shock-capturing scheme based on implementations by Cook [29] and Kawai and Lele [30] was used to thicken the shock and make it resolvable on the computational grid. This is done by applying artificial viscosity and conductivity in the regions where the shock is detected. To ensure that no artificial dissipation is introduced inside the boundary layer, the shock-capturing scheme is deactivated in the region $\psi - \psi_c < 1$ deg.

Because of the short duration of the test run, the surface of the model does not have time to heat up and thus can be assumed to be isothermal with a temperature of 300 K. For runs modeling the porous carbon/carbon surfaces, impedance boundary conditions [see Eq. (8)] were applied, controlling the transpiration velocity as a function of the wall pressure fluctuations. The value of the impedance is extracted from a pore-scale acoustic analysis called the inverse

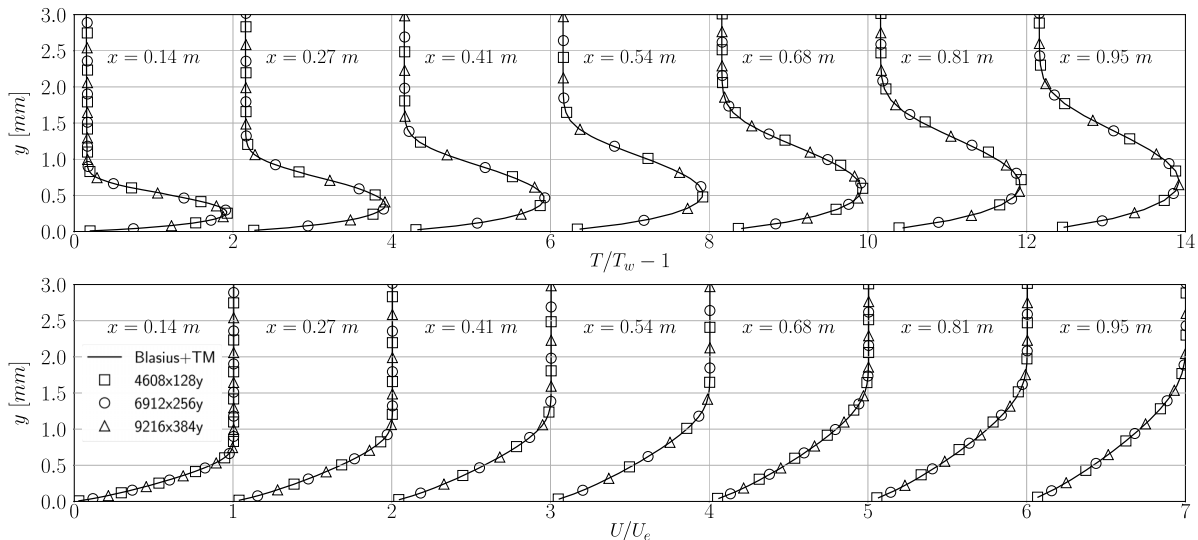


Fig. 2 Temperature and streamwise velocity profiles from the unperturbed DNS (symbols); analytical approximation combining Mangler-transformed Blasius and Taylor–Maccoll solutions (lines).

Helmholtz solver (Sec. III.B) and compared to low-order algebraic models (Sec. V.B). This approach allows to model the acoustic response of the porous surface without the need to resolve its complex geometrical structure. This strategy allows to retain high resolution on the flow side by removing the grid resolution requirements that would be needed to capture the acoustic wave propagation in the pores.

III. Computational Tools

A. High-Order Structured Compact Finite Difference Solver in Curvilinear Coordinates: CFDSU

CFDSU solves the fully compressible Navier–Stokes equations on a structured curvilinear grid using a sixth-order compact and staggered finite difference scheme [31]. Compact methods outperform conventional finite difference schemes based on spatially local discretization at high wave numbers without restricting the geometry and boundary conditions of the problem demanded by a spectral method [32,33].

The governing flow equations are solved in a curvilinear coordinate system for the contravariant components of velocity. The full set of transformed equations can be found in Nagarajan et al. [34]. Recent developments of the code at Purdue University have enabled the use of fully three-dimensional, nonorthogonal grid transformations in the code.

CFDSU has also been equipped with time-domain impedance boundary conditions (TDIBCs) based on the formalism of Fung and Yu [35] and the implementation in fully compressible Navier–Stokes codes by Scalo et al. [24]. The TDIBC formulation belongs to the class of characteristic boundary conditions [36] and is implemented based on the complex wall softness coefficient $\hat{S}(\omega)$, which is related to the reflection coefficient $\hat{R}(\omega)$ via

$$\hat{S}(\omega) = \hat{R}(\omega) + 1 \quad (5)$$

and is evaluated using the complex poles and residues that describe the IBC [see Eq. (12)] being ultimately imposed in the time domain in the Navier–Stokes calculations. Following, $\hat{R}(\omega)$ relates the incident (\hat{A}^-) and reflected (\hat{A}^+) waves (Fig. 1) in the frequency domain via

$$\hat{R} = \frac{\hat{A}^+}{\hat{A}^-} \quad (6)$$

where the time-domain definition of the incident and reflected waves is

$$\begin{cases} A^-(t) = v'(t) + \frac{p'(t)}{\rho_0 a_0} \\ A^+(t) = v'(t) - \frac{p'(t)}{\rho_0 a_0} \end{cases} \quad \text{and} \quad \begin{cases} \hat{A}^-(\omega) = \hat{v}(\omega) + \frac{\hat{p}(\omega)}{\rho_0 a_0} \\ \hat{A}^+(\omega) = \hat{v}(\omega) - \frac{\hat{p}(\omega)}{\rho_0 a_0} \end{cases} \quad (7)$$

where v' and p' are the fluctuating values of wall-normal velocity and pressure, respectively, and ρ_0 and a_0 are the base density and speed of sound of the fluid.

Adopting a harmonic convention to transform the variables to frequency domain, the specific acoustic impedance $Z_*(\omega)$ (made dimensionless via the base impedance $\rho_0 a_0$) is defined as a function

of the perturbed pressure $p'(t)$ and its induced normal velocity component $v'(t)$ into a porous surface, satisfying the relation

$$\hat{p}(\omega) = \rho_0 a_0 Z_*(\omega) \hat{v}(\omega) \quad (8)$$

Fung and Yu [35] demonstrated that it is possible to evaluate the outgoing wave by a causal convolution of the incident wave. The wall-normal velocity can then be recovered and imposed as a Dirichlet boundary condition at each time step:

$$v' = \frac{1}{2}[A^- + A^+] \quad (9)$$

The staggered variable arrangement does not place pressure nodes at the boundary and, as such, only requires condition 9 to be imposed to continue the calculations.

B. Pore-Cavity Inverse Ultrasonic Solver: Inverse Helmholtz Solver

The inverse Helmholtz solver (IHS) is a novel computational methodology that allows the evaluation of the spatial distribution of acoustic impedance at the open surface of an arbitrarily shaped cavity for a given frequency. This technique spatially integrates the linearized Navier–Stokes equations transformed into the frequency domain

$$j\omega \frac{\rho_0}{p_0} \hat{p} - j\omega \frac{\rho_0}{T_0} \hat{T} + \rho_0 \frac{\partial \hat{u}_k}{\partial x_k} = 0 \quad (10a)$$

$$j\omega \rho_0 \hat{u} + \frac{\partial \hat{p}}{\partial x} - \mu \frac{\partial}{\partial x_k} \left(\frac{\partial}{\partial x_k} \hat{u} \right) = 0 \quad (10b)$$

$$j\omega \rho_0 \hat{v} + \frac{\partial \hat{p}}{\partial y} - \mu \frac{\partial}{\partial x_k} \left(\frac{\partial}{\partial x_k} \hat{v} \right) = 0 \quad (10c)$$

$$j\omega \rho_0 c_v \hat{T} + p_0 \frac{\partial \hat{u}_k}{\partial x_k} = \kappa \frac{\partial}{\partial x_k} \left(\frac{\partial}{\partial x_k} \hat{T} \right) \quad (10d)$$

on an unstructured grid for a broad range of frequency values (where ω is a real-valued input to the solver), from the cavity walls (with assigned no-slip, isothermal conditions) up to the open surface, where the local value of impedance for each frequency is retrieved as a result of the calculation (see Patel et al. [37,38] and Wagner et al. [39] for more details).

Multiple instances of the IHS can be concurrently executed to reconstruct the full, broadband acoustic impedance at the open surface of any given geometry. Such an impedance can then be implemented as a time-domain impedance boundary condition (IBC) in flow-side-only simulations as discussed in Sec. III.A).

To apply this technique to a material composed of arbitrarily distributed geometrically complex cavities, such as a C/C block, high-resolution images are needed. The descriptive images, such as the ones shown in Fig. 3, are read as two-dimensional arrays containing grayscale values of each pixel using an image processing code written in Python. A filter is then applied wherein each pixel with a grayscale value under a given threshold is considered to be part of a pore. The images are then scanned for connected regions that



Fig. 3 Reflected-light microscopy generated images of classic (untreated) C/C (left), optimized C/C (middle), and optimized C/C-SiC (right) [50].

represent each pore, and an automatic approximation to a rectangular slot or a cylindrical hole is made based on the pore's extent in each direction. Finally, pixels are converted to micrometers and used to recover the significant dimensions of each pore, which can be used to determine the porosity and eventually the impedance of the C/C surface.

Once the surface porosity and significant dimensions of each surface pore are known, the inverse Helmholtz solver (IHS) [38] is used to evaluate the broadband surface-averaged specific acoustic impedance of each pore. These impedances are then combined, assuming that the hard walled portion of the surface has zero admittance, such that the total surface-averaged impedance of the sample is given by

$$Z_*(\omega) = \left(\sum_{i=1}^{N_{\text{pores}}} \frac{1}{Z_{i,*}(\omega)} \frac{A_i}{A_{\text{total}}} \right)^{-1} \quad (11)$$

where Z_i is the specific acoustic impedance of the i th pore, and A_i its surface area.

Time-domain impedance boundary condition (TDIBC) application requires that the acoustic impedance be specified as a set of complex poles and residues representing a superposition of causal second-order oscillators. These poles and residues are obtained by fitting the wall softness coefficient corresponding to the evaluated broadband acoustic impedance from the IHS:

$$\hat{S}(\omega) = \frac{2}{1 + Z_*(\omega)} \approx \sum_{k=1}^{n_o} \left[\frac{\mu_k}{s - p_k} + \frac{\tilde{\mu}_k}{s - \tilde{p}_k} \right] \quad (12)$$

where \hat{S} is the wall softness coefficient, n_o is the number of oscillators, μ_k is the residues, p_k is the poles, and $s = j\omega$. In Eq. (12), the superscript \sim denotes the complex conjugate.

The fit is performed following the procedure described in Lin et al. [40], where the values and quantity of poles and residues are varied iteratively while minimizing the difference between the wall softness evaluated using the impedance obtained from the IHS for a discrete set of frequencies and the one evaluated using the poles and residues obtained in the previous iteration.

IV. Analytical Models of Surface Impedance for Porous Materials

A. Homogeneous Absorber Theory

The homogeneous absorber theory (HAT) [41] models the normal impedance of a porous absorber as

$$Z_{\text{HAT}} = Z_{\infty} \frac{1 + e^{-j2k_a H}}{1 - e^{-j2k_a H}} \quad (13)$$

which corresponds to the effective impedance of the absorber when the wave propagates normal to its surface (see discussion in Sec. IV. C). The other parameters in Eq. (13) are

$$k_a = k\sqrt{\kappa} \sqrt{1 - j\frac{\omega_k}{\omega}}, \quad Z_{\infty} = Z_0 \frac{\sqrt{\kappa}}{\phi} \sqrt{1 - j\frac{\omega_k}{\omega}}$$

and ω_k , the breaking frequency, is given by

$$\omega_k = \frac{\Xi\phi}{\rho_0\kappa} \quad (14)$$

where κ is the structure factor, Ξ is the flow specific resistivity, ϕ is the volume porosity, k and $\omega = 2\pi f$ are the wave number and angular frequency of incident wave, H is the total depth of the absorber, and $Z_0 = \rho_0 a_0$ is the base impedance. The breaking frequency of the absorber can be interpreted as the (approximate) demarcation between two distinct behaviors of wave propagation inside the porous media; for $\omega \ll \omega_k$, the propagation is dispersive, and for $\omega \gg \omega_k$, there is no frequency dependency on the propagation speed of the waves.

B. Fedorov's Model for Porous Absorber Impedance

Fedorov et al. [42] used the following expression to estimate the impedance due to wave propagation through a regular porous media composed of cylindrical holes with axes oriented normal to the surface (and aligned with the wave propagation direction):

$$Z_{\text{fedorov}} = Z_0 \left(\frac{\phi}{Z_{\infty,*}} \tanh(\Lambda H) \right)^{-1} \quad (15)$$

where Λ is the propagation constant, whose dimensions are the inverse of a length. Fedorov et al. [8] extended the model to porous media with random porous structure through the use of the nondimensional dynamic density ρ_{dyn}^* and the nondimensional dynamic compressibility C_{dyn}^* based on previous theoretical work performed by Johnson et al. [43] and Allard and Champoux [44]. In his 2003 publication [8], Fedorov et al. nondimensionalized the resulting expression for the impedance of the metal felts in a manner consistent with his LST framework. Because we are interested in comparing his model with the current IHS and HAT predictions, we recast some of equations and parameters of his model in the following form:

$$\begin{aligned} Z_{\infty,*}(\omega) &= \sqrt{\rho_{\text{dyn}}^*(\omega)/C_{\text{dyn}}^*(\omega)}, \quad \Lambda(\omega) = j\omega \sqrt{\rho_{\text{dyn}}(\omega)/K_{\text{dyn}}(\omega)}, \\ \rho_{\text{dyn}}^*(\omega) &= \kappa \left[1 + \frac{g^*(\lambda_1^*)}{\lambda_1^*} \right], \quad C_{\text{dyn}}^*(\omega) = \gamma - \frac{\gamma - 1}{1 + g^*(\lambda_2^*)/\lambda_2^*}, \\ \rho_{\text{dyn}}^* &= \rho_{\text{dyn}}(\omega)/\rho_w, \quad C_{\text{dyn}}^*(\omega) = \gamma P_w/K_{\text{dyn}}(\omega), \\ g^*(\lambda) &= \sqrt{1 + \frac{4\kappa\mu\lambda^*}{\Xi\phi r_p^2}}, \quad \lambda_1^* = \frac{j\kappa\rho_w\omega}{\phi\Xi}, \\ \lambda_2^* &= 4Pr\lambda_1^*, \quad \text{and} \quad r_p = s_h \sqrt{\frac{8\mu\kappa}{\Xi\phi}} \end{aligned}$$

where the symbol $*$, being a superscript or a subscript, refers to nondimensional quantities (and not to the complex conjugate). All of the parameters present in these equations variables have been previously defined except for $K_{\text{dyn}}(\omega)$, which is the dynamic bulk modulus relating the divergence of the average molecular displacement of the gas to the average pressure variation; r_p , which is the characteristic size of the pores; and s_h , which is a shape factor that accounts for the anisotropy of the pores. As a way of estimating the shape factor for the current C/C samples, and consistently with Fedorov et al. [8], we treat r_p as a hydraulic radius (i.e., the ratio of the doubled pore area to the pore perimeter at the surface). With this assumption, we use Fig. 3 to visually estimate the shape factor for the classical C/C sample obtaining $s_h \approx 1.26$. The Prandtl number Pr is taken to be 0.704.

In Fedorov et al. [8], the propagation constant multiplied by the depth ΛH (made dimensional here) was expressed as proportional to $j\omega H \sqrt{\rho_{\text{dyn}}(\omega)K_{\text{dyn}}(\omega)}$, whereas in Allard and Champoux [44], it was expressed as $\Lambda H = j\omega H \sqrt{\rho_{\text{dyn}}(\omega)/K_{\text{dyn}}(\omega)}$. The latter is the expression adopted herein because we believe that what was reported in Fedorov et al. [8] is a mere typographical error. For porous absorbers with high flow resistivity Ξ , coincidentally both expressions yield similar overall impedances due to the asymptotic nature of the hyperbolic tangent function.

C. Wave Angle Effects on Acoustic Absorption

The wave angle is an important factor significantly affecting the overall acoustic performance of the absorber. This is typically taken into account, with the assumption of a locally reacting surface, as a correction to the value of the normal impedance, yielding the effective impedance

$$Z_{\text{eff}}(\omega) = Z(\omega) \cos(\theta_i) \quad (16)$$

ultimately used in linear acoustic relations to predict the absorption coefficient β , given by

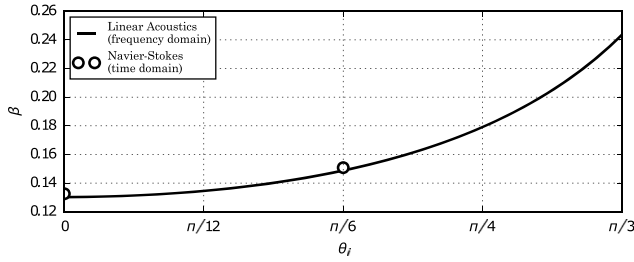


Fig. 4 Influence of incidence angle θ_i in the absorption coefficient β for $f = 300$ kHz, $p_0 = 10$ kPa, and $T_0 = 300$ K.

$$\beta(\omega) = 1 - \left(\frac{|\hat{A}^+|}{|\hat{A}^-|} \right)^2 = 1 - \left| \frac{1 - Z_{\text{eff},*}(\omega)}{1 + Z_{\text{eff},*}(\omega)} \right|^2 \quad (17)$$

which is evaluated by comparing the amplitude of the incident wave $|\hat{A}^-|$ to the reflected wave $|\hat{A}^+|$, representing a figure of merit of the absorber.

The cosine term in Eq. (16) accounts for the wave incidence angle θ_i , intended as zero when the direction of wave propagation is normal to the surface of the absorber; $Z(\omega)$ is hence intended as the normal impedance and is the only one that should be imposed in Navier–Stokes calculations with time-domain impedance boundary conditions (TDIBC). To verify this, we have performed two-dimensional Navier–Stokes calculations, mimicking Wagner et al.’s bench-test experiments [39], where a quasi-planar acoustic wave was introduced through a source term controlling the main propagation direction angle. Although the experimental setup was constructed to measure waves with angle of incidence of $\theta_i = 30$ deg, we also performed a simulation of a wave normal reflection.

Figure 4 shows a comparison between the absorption coefficient predicted via the cosine correction [see Eq. (17)], that is using the effective value of impedance [Eq. (16)] and the Navier–Stokes calculations, showing very good agreement. It is important to stress that the IBCs imposed in the Navier–Stokes calculations 1) only affect the inviscid wall-normal flux, and 2) only impose the normal impedance, i.e., values of impedance as predicted by Eq. (13) or Eq. (15) and not the effective value, that is Eq. (16).

V. Results

The goal of this section is to reproduce and analyze the disturbance amplification mechanism in a hypersonic flow over a sharp cone with impermeable smooth walls through the excitation of the boundary layer with a broadband frequency pulse. Then, we model the acoustic response of real C/C materials through the IHS technique (Sec. III.B), compare it against impedance estimates from low-order acoustic models as well as bench-test data from the ultrasonic measurements by Wagner et al. [39], and ultimately test its attenuation capability by assigning the predicted impedance as a boundary condition to Navier–Stokes calculations, which allows a comparison with the tests conducted in HEG with a C/C porous insert.

An approximate steady laminar solution obtained by blending of the compressible Blasius boundary-layer solution applied to a supersonic sharp cone [26,28] with the inviscid Taylor–Maccoll [25] flow is introduced in the Navier–Stokes calculation both as an inlet and initial condition. After initialization, the inputted solution

needs to adapt to the discretized full Navier–Stokes equations. The boundary-layer profiles at various locations after this (merely numerical) transient adjustment are shown in Fig. 4 for $Re_m = 4.06 \cdot 10^6 \text{ m}^{-1}$; excellent matching between the approximate solution and the steady Navier–Stokes calculations is observed. The same degree of agreement was also achieved for the lower-Reynolds-numbers cases (not shown). As shown in Table 2, the highest Reynolds number is the most stringent case in terms of grid requirements. Given the long streamwise extent of the computational domain, the accuracy of the boundary-layer profiles toward the end of the cone is very sensitive to the degree of numerical dissipation. In fact, preliminary runs with more dissipative settings of numerical filtering have shown to overpredict the boundary-layer thickness for large values of x .

A. Broadband Pulse Disturbance Introduction and Amplification over Smooth/Impermeable Wall

After the establishment of an unperturbed steady base state, controlled velocity disturbances with an amplitude of 1 m/s are imposed via suction and blowing at the wall for a finite amount of time ($1.67 \mu\text{s}$) and in a finite-length interval ($x = 0.14 \pm 0.0036 \text{ m}$) following the expression (in meters per second):

$$v(x, y = 0, t) = \cos(\pi\xi)^3 \sin(2\pi ft), \quad \text{for } 0 \leq t \leq 1/f \quad (18)$$

where ξ is a variable with values ranging in $[-1, 1]$, which is mapped to the actual spatial interval of application of the pulse, and $f = 600$ kHz is the frequency around the which the pulse spectrum is centered. This perturbation aims at mimicking a natural transition scenario as well as helping identifying the most-amplified frequency inside the boundary layer as a function of the streamwise position on the surface of the cone. It was first used by Gaster and Grant [45] in incompressible boundary-layer transition simulations and by Sivasubramanian and Fasel [46] in hypersonics.

Figure 5 shows the pressure time series at the wall for different streamwise locations. A rapid amplification of the overall pressure signal is observed initially, from $x = 0.15 \text{ m}$ up to approximately $x = 0.25 \text{ m}$, followed by a later gentler growth. However, the total disturbance amplitude contains energy at various frequencies, and although the pulse excitation inputs a similar amount of energy in all the frequencies range relevant to the boundary-layer instability, some of the components experience a long region of decay before reaching their unstable region (Fig. 6). In the end, the overall amplitude of the signal depends on the balance between the attenuation in the stable region and the overall integrated growth in the unstable region of each frequency component. In fact, consistent with amplification dynamics of instability waves in (canonical) hypersonic boundary layers, higher-frequency modes experience growth earlier (i.e., where the boundary layer is thinner and, simultaneously, the remaining frequency components are attenuated).

The early rapid overall pressure signal amplitude increase is hence due to the high-frequency component, in the range of 800 kHz for $Re_m = 4.0 \times 10^6$, of the inputted broadband disturbance pulse. After this initial phase, a rapid decay is also observed due to the fast evolution of the boundary-layer thickness in its early stages, which changes the quickly unstable frequency band. At last, the later gentler growth shown in Fig. 5 happens because, as the signal moves downstream, the boundary-layer thickness evolution becomes

Table 2 Grid resolution metrics for the three Reynolds numbers chosen in this paper

Re_m, m^{-1}	1.46×10^6			2.43×10^6			4.06×10^6		
n_x	4608	6912	9216	4608	6912	9216	4608	6912	9216
n_y	128	256	384	128	256	384	128	256	384
$(\Delta x/\delta)_{0.14m}$	0.1560	0.1080	0.0809	0.2354	0.1637	0.1225	0.2746	0.1814	0.1383
$(\Delta x/\delta)_{0.95m}$	0.0591	0.0403	0.0304	0.0922	0.0605	0.0451	0.1006	0.0689	0.0506
$(\Delta y_{\min}/\delta)_{0.14m}$	0.0137	0.0070	0.0046	0.0207	0.0106	0.0070	0.0242	0.0117	0.0079
$(\Delta y_{\min}/\delta)_{0.95m}$	0.0363	0.0182	0.0121	0.0566	0.0273	0.0180	0.0618	0.0311	0.0202

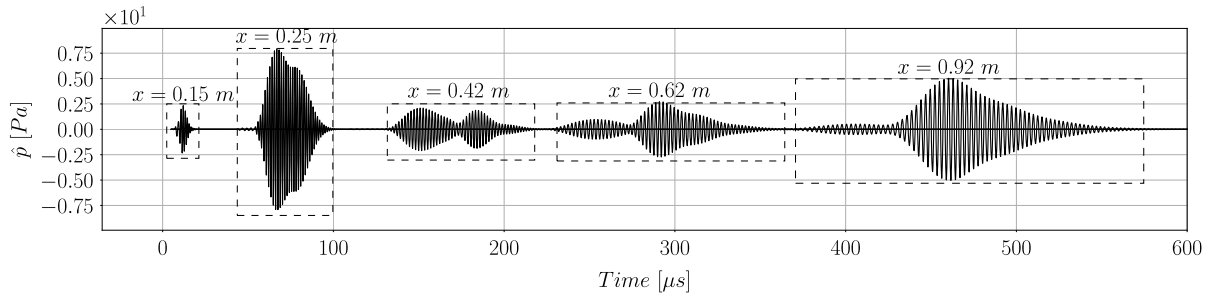


Fig. 5 Time series of the pressure perturbation at different streamwise locations for $Re_m = 4.06 \times 10^6 \text{ m}^{-1}$ with a $n_x = 9216$ and $n_y = 384$.

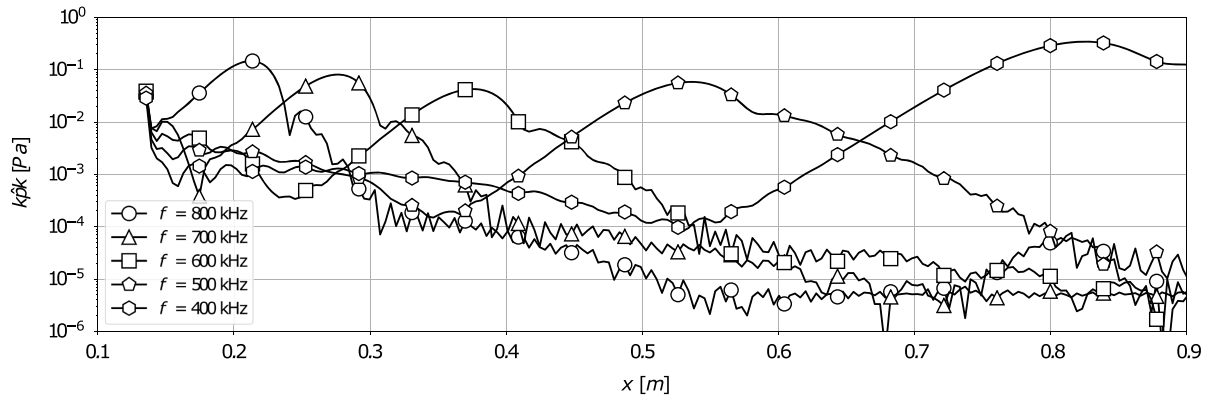


Fig. 6 Amplitude of pressure disturbance at the wall for different frequency components with $n_x = 6912$, $n_y = 256$, and $Re_m = 4.0 \times 10^6 \text{ m}^{-1}$.

slower, and the overall integrated growth becomes steadily bigger than the initial attenuation.

A Fourier analysis of such times series is shown in Fig. 7, demonstrating that, for all Reynolds numbers considered, the initial broadband characteristic of the signal is very rapidly lost, and the power spectrum concentrates in a narrow band of ultrasonic frequencies, consistent with second-mode amplification mechanisms for each flow conditions considered. Experimental studies conducted by Stetson [47] confirmed the validity of the following estimation for the second-mode frequency:

$$f = \frac{U_e}{2\delta} \tag{19}$$

where U_e is the boundary-layer edge velocity, and δ is the boundary-layer thickness, defined as the wall-normal distance where $u \simeq 0.999U_e$. Predictions based on Eq. (19) are plotted in Fig. 7, showing good agreement with the DNS results. A detailed phase speed analysis reveals that both slow and fast modes [48] are observed in the current DNS; however, most of the disturbance energy and growth are carried by the slow mode (not shown),

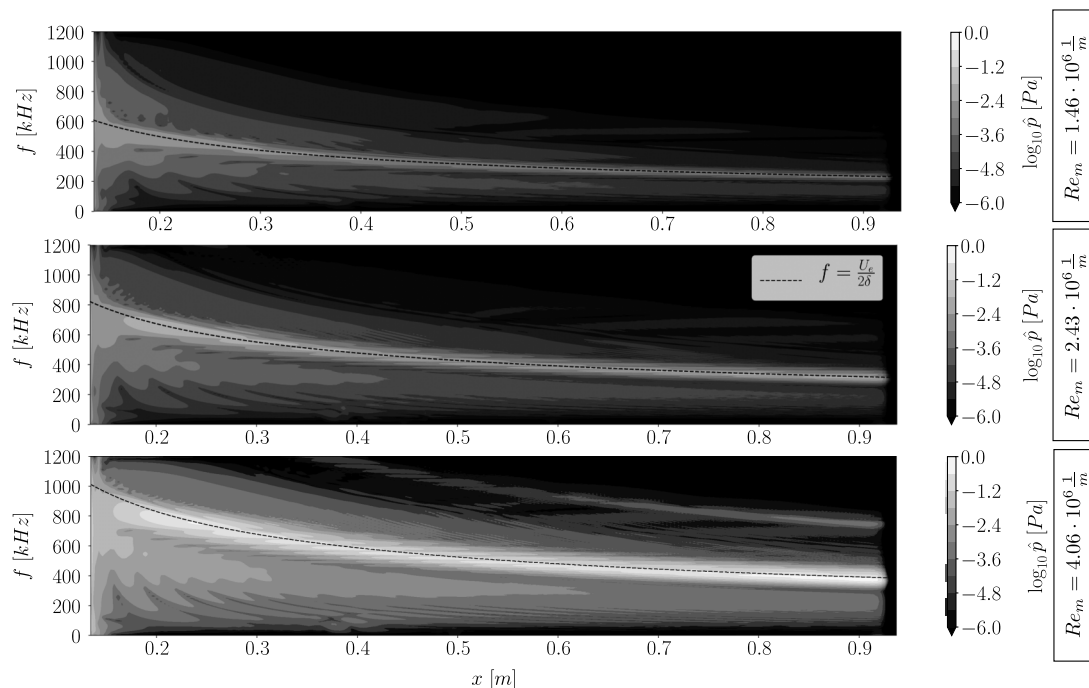


Fig. 7 Contours of Fourier-mode amplitude as a function of frequency and space for the three Reynolds numbers considered and $n_x = 6912$ and $n_y = 256$.

corresponding to Mack's second mode after the phase speed synchronization point (see discussion on terminology of instability modes in Egorov et al. [21]).

The broadband pulse excitation is able to capture the correlation between the most-amplified frequencies in the boundary layer and its thickness revealing information similar to stability analysis. It is observed that the second-mode frequency follows closely the boundary-layer thickness; the higher the Reynolds number is, the thinner the boundary layer is and the higher the excited frequencies are. Figure 8 shows pressure isosurfaces near the surface of the cone, reminiscent of acoustically channeled waves with some power

transmitted (or lost) outward through the sonic line, characteristic of the second mode (Egorov et al. [21]).

Another phenomenon that occurs as the imposed pulse advects downstream is that its magnitude becomes large enough to excite higher harmonics. For the high Re_m case, specifically, the appearance of the first harmonic of the second mode is visible after $x = 0.7$ m, shown in Fig. 9. At the very end of the computational domain, a sponge layer, starting around $x = 0.94$ m, damps the imposed disturbances before they reach the outflow boundary condition. No sign of spurious upstream disturbances has been identified in the subsonic part of the boundary layer near the outflow.

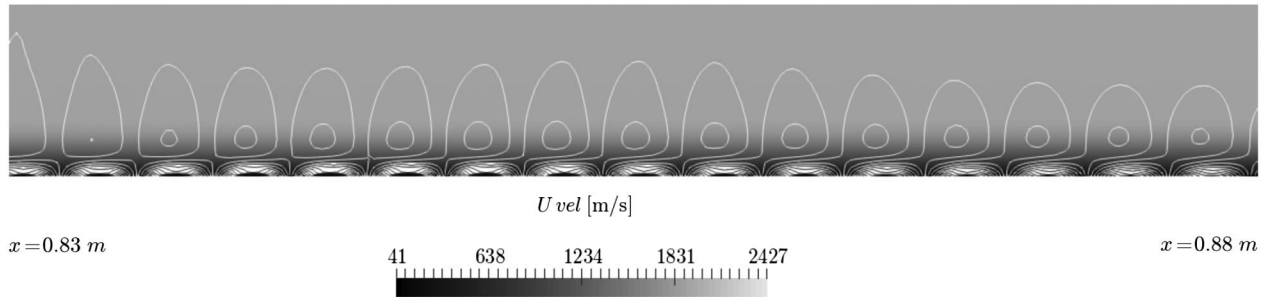


Fig. 8 Pressure oscillation isosurfaces in the boundary-layer region for $n_x = 4608$, $n_y = 128$, and $Re_m = 4.0 \times 10^6 \text{ m}^{-1}$.

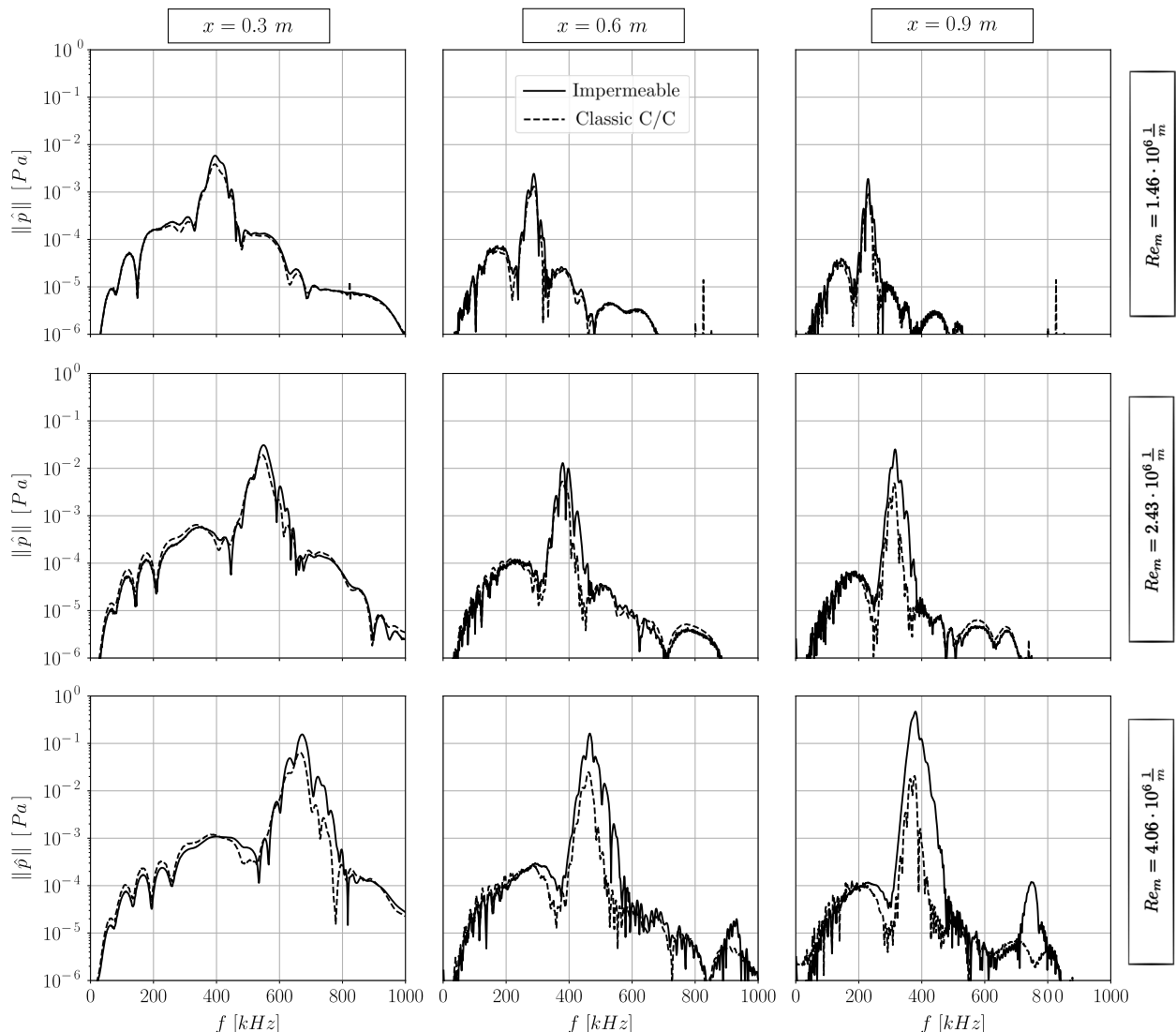


Fig. 9 Frequency domain distribution of the power spectrum at the wall for different streamwise locations in the advection of broadband pulse simulations over porous and impermeable walls.

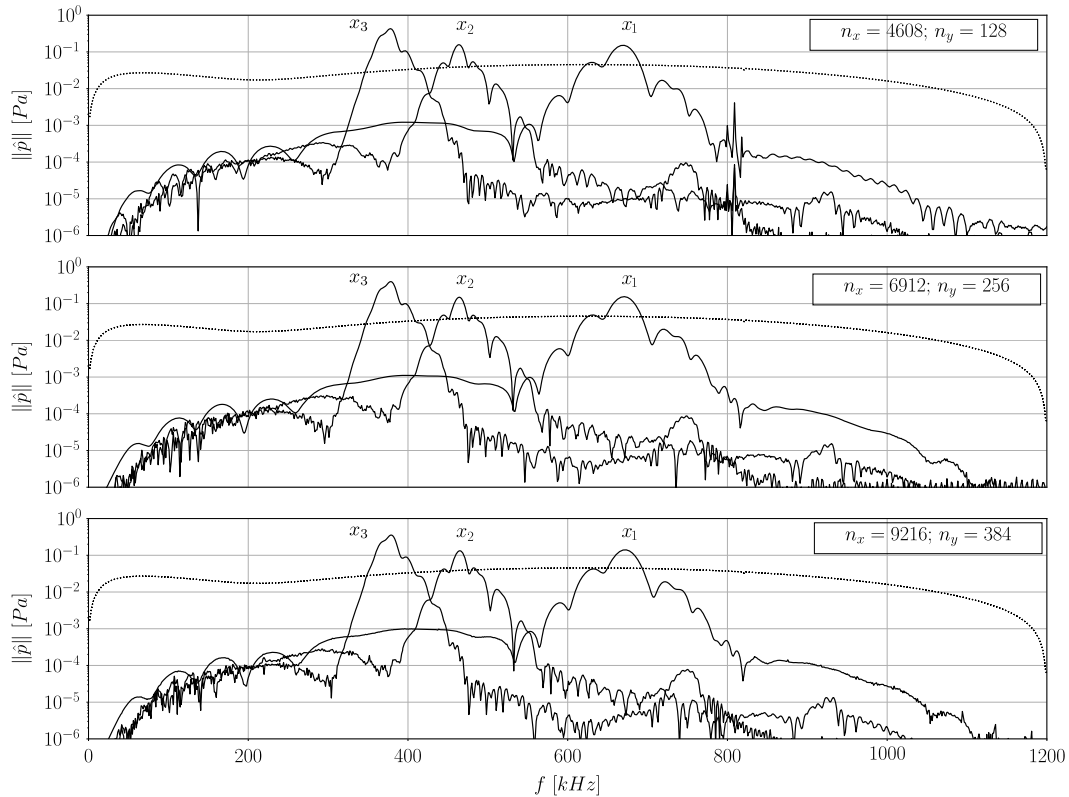


Fig. 10 Grid convergence analysis for the perturbation spectrum at $x_1 = 0.3$ m, $x_2 = 0.6$ m, and $x_3 = 0.9$ m in an axisymmetric simulation of broadband pulse propagation at $Re_m = 4.06 \times 10^6 \text{ m}^{-1}$.

The spatial resolution and the numerical discretization strategy play a crucial role in the quality of the prediction of the evolution dynamics of high-frequency perturbations, such as second-mode waves. The grid convergence study in Fig. 10 demonstrates adequate spectral resolution on the intermediate grid adopted ($n_x = 6912$, $n_y = 256$); results on the coarser grid ($n_x = 4608$, $n_y = 128$) are also adequate, with the exception of spurious energy accumulation at $f = 800$ kHz. The latter is actually due to a numerical disturbance originating from the interaction of the inflow sponge layer and the coarse grid as well as insufficient resolution of the propagating waves. This spurious wave source propagates into the domain and is not damped due to the low artificial diffusion of the scheme. Although the dynamics of the disturbance evolution inside the conical hypersonic boundary layer are not altered by this spurious perturbation, only intermediate or high resolutions ($n_x \geq 6912$, $n_y \geq 256$) of such full cone axisymmetric computations will be considered.

The finest grid resolution available ($n_x = 9216$, $n_y = 384$) is capable of adequately resolving wavelengths of 0.8 mm, assuming a minimum requirement of eight points per wavelength for compact finite difference schemes. With the boundary-layer thickness toward the end of the cone of the order of 2 mm, this resolution is not adequate to capture the nonlinear breakdown to turbulence. The effects of porous walls on the latter will be investigated in future computations focused on (inevitably) shorter sections of the cone.

B. Impedance Characterization of Carbon-Fiber-Reinforced Carbon Ceramics (C/C) Materials

Carbon/carbon silicon carbide (C/C-SiC) is a material that has already been used as a thermal protection system (TPS) in hypersonic flight [15,16]. C/C represents an intermediate state of its manufacturing process. The porosity of C/C materials is a result of thermal stresses that appear in the cooldown process of the material after pyrolyzation of the matrix. This material offers excellent thermal resistance, low expansion, and specific weight as well as high temperature stability in nonoxidizing atmospheres. However, C/C cannot be used when the oxidizing effects are important in the flow without a protective

treatment. Resistance against oxidation is acquired by the infiltration of a liquid phase of silicon into the porous carbon, followed by a reaction to SiC. If this infiltration is done in the untreated C/C, its microstructural gaps will be filled and the acoustic absorption properties of the material lost.

To solve this problem, DLR Stuttgart developed a technique that is able to selectively insert cavities into the C/C structure by replacing carbon fibers with a nonstable material that will degrade after the pyrolyzation step in the desired locations, which allowed to nearly double the porosity [49]. The existence of larger gaps in this optimized C/C (Fig. 3) allows it to retain a certain porosity degree after the SiC reaction. This results in the optimized C/C-SiC, which combines the properties of oxidation resistance with acoustic absorption [50].

The complex acoustic impedance of the classic C/C sample shown in Fig. 3 was estimated via various methodologies with results shown in Fig. 11. The acoustic analysis of the optimized C/C and C/C-SiC are deferred to future work.

Experimentally determined and theoretically predicted values of β Eq. (17) are plotted in Fig. 12. The experimentally determined absorption coefficient by Wagner et al. [39] was obtained by comparing the amplitude of a wave reflected off an acoustically absorptive surface to the same wave reflecting off a purely reflective (impermeable) boundary. This absorption process is a function not only of the porous absorber but also of the flow properties themselves; for example, it will depend on the angle of incidence, which will change the effective impedance $Z_{\text{eff},*}(\omega)$, which should be used to evaluate β . To enable comparison between the experiments performed by Wagner et al. [39], all the results presented in Figs. 11 and 12 consider an angle of incidence of $\theta_i = 30$ deg.

The predictions of acoustic impedance evaluated using the inverse Helmholtz solver (IHS) are compared with experimental results of bench-test acoustic characterization of ultrasonically absorptive porous samples [39] and two different theoretical models: 1) the homogeneous absorber theory (HAT) detailed in Möser [41] and used by Wagner [13], and 2) the model for acoustic impedance of a porous surface with random porosity used by Fedorov et al. [8] in his LST

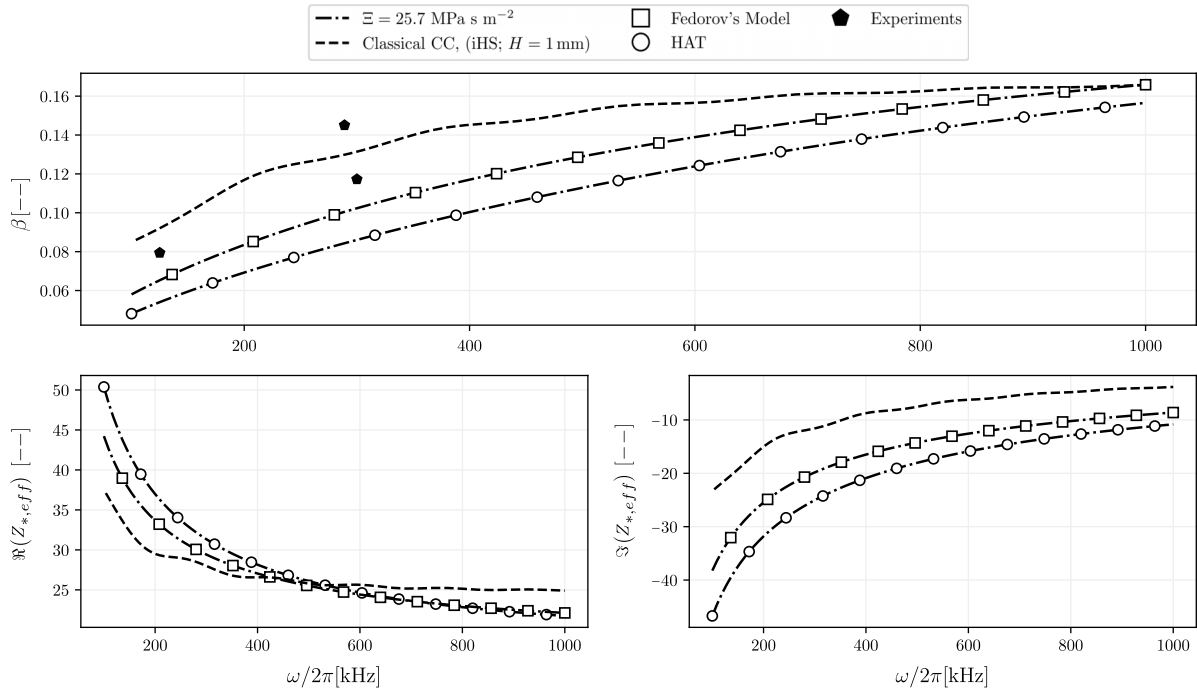


Fig. 11 Comparison of real $\Re(Z_{*,\text{eff}})$ and imaginary $\Im(Z_{*,\text{eff}})$ parts of the specific impedance $Z_{*,\text{eff}}(\omega)$ and absorption coefficient β obtained from various models at $\theta_i = 30$ deg and wall conditions corresponding to $Re_m = 4.06 \times 10^6 \text{ m}^{-1}$.

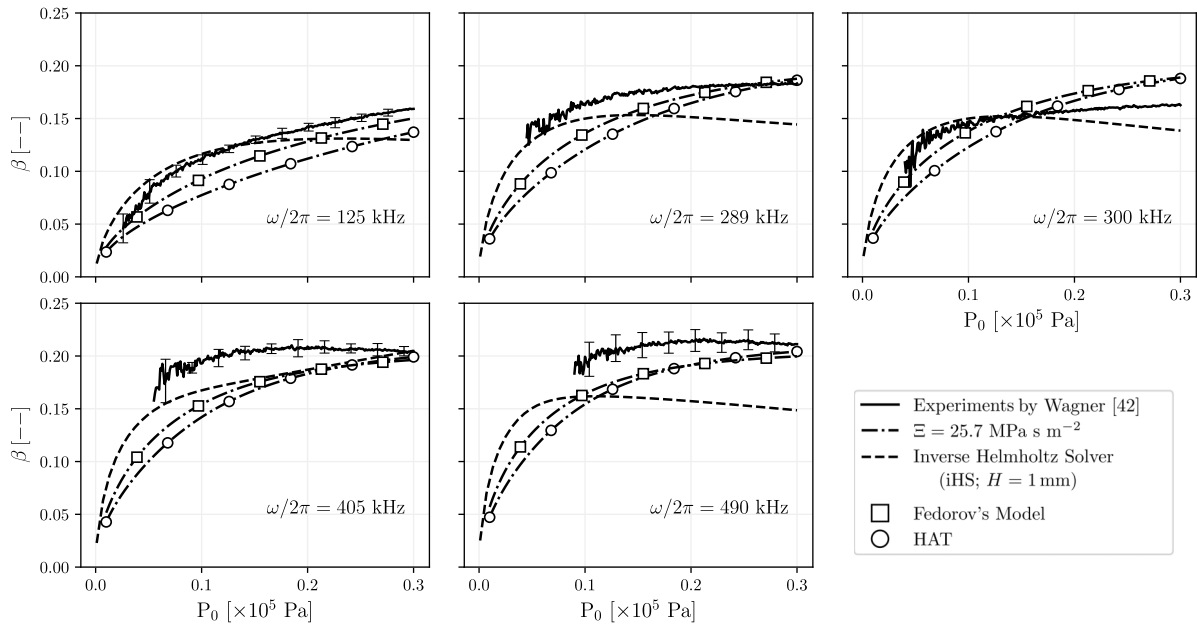


Fig. 12 Comparison of measured and predicted absorption coefficient β for the classical C/C vs base pressure.

calculations of second-mode attenuation over a felt metal coatings. Both these models have been briefly summarized in Sec. IV.

The use of these models relies on the determination of physical parameters that describe some characteristics of the flow through the porous medium such as: the porosity ϕ , which is the ratio of the pore volume to the total volume; the flow resistivity Ξ , which represents the resistance (pressure difference) to the flow of air through the medium; and the structure factor κ , which accounts for the presence of some “blind” and tortuous paths in the absorber. Wagner [13] in 2014 reported for the first time the values that characterize the classical C/C material, which are summarized in Table 3. Although ϕ and Ξ can be experimentally obtained [51], κ cannot be measured or calculated directly for randomly structured porous materials, and it was inferred from the experimentally measured reflection coefficient. In 2018 DLR has remeasured the flow resistivity Ξ of the classical C/C

sample, reporting a value almost double what was previously published. The reason for the difference in the measured Ξ was attributed to the better sealing of the samples (the edge of the samples was galvanized with copper to avoid leakage) in the more recent experiments. Results from these new measurements are also reported in Table 3 and will be the one used in the present analysis to inform the choice of parameters in the HAT and Fedorov’s model.

Table 3 Properties of the porous absorber investigated

Experiment	ϕ	κ	$\Xi, \text{MPa} \cdot \text{s} \cdot \text{m}^{-2}$	Depth H, m
Wagner (2014) [13]	0.15	8.0	13.3	5.0×10^{-3}
DLR (2018)	0.15	8.0	25.7	5.0×10^{-3}

The acoustic characterization experiments by Wagner et al. [39] provide wave absorption data for a discrete set of frequencies because a different transducer receiver pair is needed for testing different frequencies. However, to execute the implementation of TDIBC, a continuous reconstruction of the complex impedance in the frequency domain is required. Wagner's data are hereby compared against various acoustic absorption models to assess their predictive capability both in the form of complex impedance versus frequency at one pressure corresponding to flow conditions of $Re_m = 4.06 \times 10^6 \text{ m}^{-1}$ (Fig. 11) and in the form of absorption coefficient β at various frequencies versus pressure (Fig. 12).

For the predictions carried out numerically by the IHS methodology, a blind-hole porosity assumption was used. A surface (and hence also volume) porosity of 0.078 is used, as obtained from the processing of the high-resolution C/C surface images. A nominal depth of $H = 1 \text{ mm}$, common to all pores, has been assumed based on visual inspection of depthwise slices of a C/C sample provided by DLR Stuttgart [38].

For the chosen value of flow resistivity $\Xi = 25.7 \text{ MPa} \cdot \text{s} \cdot \text{m}^{-2}$, both the HAT and Fedorov's model underestimate the absorption coefficient at low base pressures and relative to the IHS predictions. As the pressure increases, the absorption coefficient prediction based on the IHS starts to deviate from the experimental data, and both low-order models provide better (but still not satisfying) predictions. An overall underprediction of the magnitude of the absorption coefficient is observed by all models.

The discrepancy of IHS results is attributed to the underestimated volume porosity given that only a limited selection of the largest visible pores in Fig. 3 (left) were used for the direct impedance estimate. This leads us to conclude that the smaller pores, which were ignored in the selection surface porosity estimate step (Sec. III.B), play an important role in the absorption. The latter contribution is, on the other hand, captured by low-order models for porous acoustic absorbers, especially at higher pressures. In the end, because the experiments performed in the HEG at DLR go up to a maximum pressure of $0.1 \times 10^5 \text{ Pa}$, the IHS is a better predictive tool than the theoretical models limited to the range of pressures reproduced by the DNS results in the present manuscript.

It is also worth noting that, although the acoustic impedance estimate by the use of the theoretical models presented by Fedorov and the HAT explicitly accounts for the influence of the thickness of the absorber, the high magnitude of flow resistivity Ξ of this material, in the order of $10 \text{ MPa} \cdot \text{s} \cdot \text{m}^{-2}$, results in unchanged absorption characteristics for $H \geq 1 \text{ mm}$ (i.e., the absolute thickness of the absorber for such high values of Ξ becomes irrelevant for thicknesses larger than 1 mm). This also implies that the absorbed wave is evanescent with respect to the depth of the absorber (infinitely thick absorber model), and wave reflection from the impermeable backing of the absorber is not important. Another observation is that the use of a lower flow resistivity Ξ value, such as the (now obsolete) value measured by Wagner [13] in 2014, would lead to a higher absorption coefficient and hence an unexpected better agreement with the measured absorption coefficient than the more recently obtained value.

Figure 11 compares complex impedance prediction of various models versus frequency at one given base pressure $p_0 = 5076 \text{ Pa}$. Because of the difficulty of measuring the propagation and reflection of an ultrasonic wave at low pressures and because of the need for a separate transducer/receiver pair for each frequency, only a few experimental data points could be included in these plots. These points are not sufficient to make a statement on which is the best way of predicting the complex impedance trend versus frequency, but they reiterate the previous observations that the IHS is more accurate in this low-pressure regime than the other low-order models and that a lower flow resistivity Ξ value would lead to a better agreement of the low-order acoustic models with the experimental data.

A word of caution regarding the adoption of the various models analyzed herein is that none of them take into account impedance changes due to grazing flow effects; the latter, however, are expected to be negligible due to the small size of the pores. Minimal-unit pore-resolved simulations are currently ongoing to assess this effect. It is also important to note that the evaluated specific impedance Z_* ,

despite being dimensionless, is a function of the thermodynamic base state. The impedance estimates presented here were obtained for the pressure conditions at the surface of the cone model (i.e., the conditions after the conical shock, at the wall as predicted by the inviscid Taylor–Maccoll solution) and depend on the Reynolds numbers as seen in Table 1 (see the p_e value, which corresponds to the pressure at the wall, and hence within the C/C pores). In conclusion, the effective impedance of the C/C surface is a function of the thermodynamic state of the gas that fills the C/C pore space and is hence directly relatable to the external flow conditions.

C. Porous Walls and Second-Mode Attenuation

Once we have modeled the acoustic energy absorption at the wall for the different C/C samples, we are able to input this information in the DNS as a complex impedance boundary condition. Only the impedance estimates from the IHS methodology are taken into considerations for the current sets of runs. Simulations with IBCs are run quiescent first, and then, after spurious transient waves due to initialization errors are convected out of the domain, a broadband pulse is applied via suction and blowing at the wall [Eq. (18)], with results shown in Fig. 13.

The effects of frequency and Reynolds numbers on the evolution of the Fourier mode of pressure are analyzed. It is noted that, for all cases considered, the disturbance energy for the impermeable wall case and for the porous case start at the same level and keep the same amplitude relative to each other before the impedance strip starts (denoted by the vertical dotted line). Once the pulse is advecting over the impedance boundary, acoustic energy is being extracted from the signal, and its amplitude falls below the impermeable-wall baseline until the end of the domain. It is observed that the second mode experiences higher attenuation rates due to the C/C in the regions where the mode is already stable and lower growth rates in the regions of instability for the advection over the porous walls in comparison with the run over solid walls. The combination of these phenomena leads to the decrease in the maximum power content for each frequency throughout the domain and depicts the capability of ultrasonic absorbing coating to dampen the second-mode instability in a hypersonic boundary layer. Another noticeable behavior is that the location of the maximum pressure amplitude moves upstream due to the porous walls.

Low-amplitude short-wavelength oscillations are observable at high Reynolds numbers at the later stages of the second-mode evolution (in Fig. 13). Such spatial variations in the amplitude of the Fourier modes of pressure at the wall, $\|\hat{p}\|$, may indicate the presence of a short-wavelength standing wave or spatial modulation of that particular temporal frequency, or nonlinear spectral broadening. These oscillations cannot be attributed to lack of grid resolution (see Fig. 10), and their origin will be scrutinized in more detail in future work.

Figure 9 shows the power spectrum at a given streamwise location on the surface of the cone to see how it is distributed over the frequency domain, for all the Reynolds numbers considered in this study. In this plot, we observe that the effectiveness of the porous walls in absorbing energy starts to become relevant for frequencies above 200 kHz and that the maximum amplitude of the power spectrum attenuated at the three different probed locations for all Reynolds numbers occurs beyond this frequency. The effectiveness of the attenuation of the spectrum induced by the porous surfaces increases with Reynolds numbers. The reason for this interesting behavior is believed to be because of the shift of the spectrum to higher frequencies, and because all acoustic models presented predict that the absorption coefficient of the C/C-based materials increase with frequency, the UAC becomes more effective.

Wagner [13] reported a similar behavior in his transition delay experiments in the HEG tunnel at DLR Göttingen but for a different range of Re_m . He observed that, as the Reynolds numbers increased from $4.0 \cdot 10^6$ to $9.8 \cdot 10^6 \text{ m}^{-1}$, the relative transition delay on the porous surface increased from 0.15 to 0.29. With the same reasoning, we speculate that the reason the experiments conducted by Willems et al. [52] were not able to measure any attenuation of the second-mode waves with the same C/C sample from DLR is that the

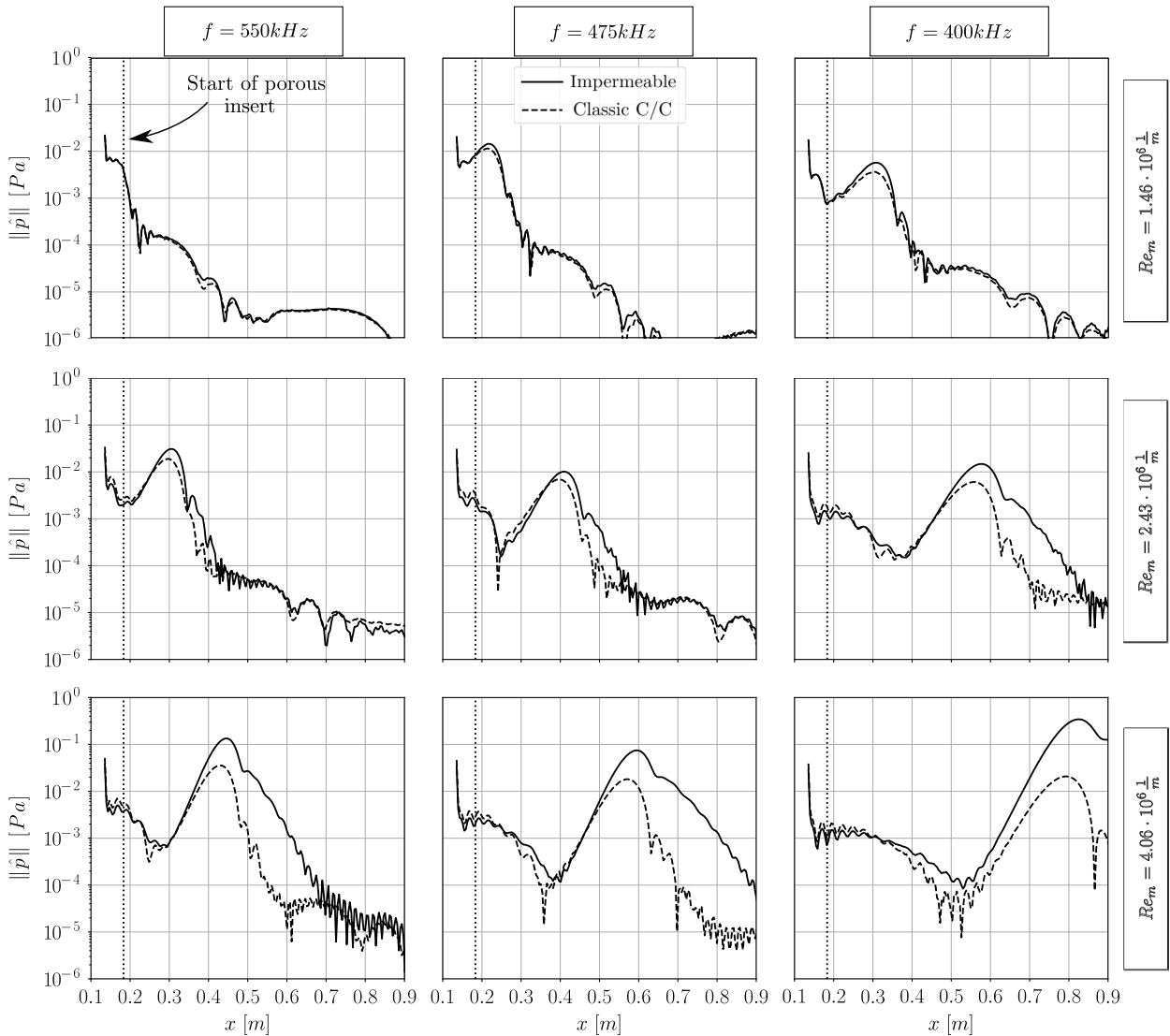


Fig. 13 Spatial distribution of the Fourier transform of pressure fluctuations at the wall for different frequencies in the broadband-pulsed simulations over porous and impermeable walls.

frequency of the second-mode waves were approximately 100 kHz at the flow conditions chosen for that study. Another factor that could have influenced the results are the very low pressures (from 0.003×10^5 to 0.008×10^5 Pa) at which the tests by Willems et al. were carried. These pressure levels lead to low absorption coefficients (shown in Fig. 12).

Other evidence of the hypersonic boundary-layer transition delay capability of acoustic energy absorption can be found at the farthest downstream probed location of the highest Reynolds number. At this position, the advection of the broadband pulse over impermeable walls was amplified to the point that started to excite the first overtone (or harmonic) of the second-mode waves. However, the presence of porous walls dampens such high-frequency modes more effectively than the second mode itself (which cascades energy onto the higher modes due to nonlinear effects, when present). This means that the disturbance with the same initial amplitude would need to propagate farther downstream to reach the necessary strength to trigger transition into turbulence effectively delaying transition.

VI. Conclusions

The effect of realistic acoustically absorptive surfaces on the second mode in a hypersonic boundary layer over a sharp slender cone was numerically studied in the present work. High-order simulations informed by the analytical relations of that describing the supersonic viscous flow of a perfect gas over a sharp cone were

performed, and the high-order simulations were capable of holding the solution and matching accurately the shape and growth of the boundary-layer profiles as they moved downstream of the cone. In addition, a novel technique (IHS) was used to solve the acoustic response at the mouth of the cavities present in porous materials and to model their collective influence through a surface averaging. The complex impedance obtained as a result was used to model the impact of the ultrasonically absorptive surface in a spatially developing boundary-layer simulation without having to resolve the intricate porous structure. The result of this simulation was then compared with previously published theoretical models, and a better agreement with experimental data for the low-pressure domain is achieved.

Artificial disturbances were introduced in the boundary layer, and their evolution with downstream advection was observed. With the introduction of a broadband pulse and its advection over a solid surface, it was possible to identify the second-mode dynamics over an impermeable wall, used as a baseline, and over materials currently being developed to be used in hypersonic transition control such as the “classical” C/C. In conclusion, for the frequencies and flow condition tested, the C/C was found capable of attenuating the second-mode and delaying boundary-layer transition into turbulence.

All results shown in the present contribution are for a sharp-tip cone. The presence of a nonnegligible tip, bluntness increases the boundary-layer thickness (for the same freestream conditions) and hence lowers growth rates and the frequency of second-mode waves. Although this will lower the effectiveness of the acoustic absorption

properties of the porous walls, resulting in a less-effective attenuation of second-mode waves, we would be still in a suitable region for the tested C/C porous material.

Acknowledgments

We acknowledge the support of the Rosen Center for Advanced Computing at Purdue University, the U.S. Air Force Office of Scientific Research (AFOSR) grants FA9550-16-1-0456 and FA9550-16-1-0209, the AFOSR Young Investigator Program 2018 award (FA9550-18-1-0292), and the National Science Foundation (NSF) Fluid Dynamics Program award (00068647). We acknowledge the very fruitful discussions with Ivett Leyva (AFOSR), Eric Marineau (Office of Naval Research), Steven Schneider, and all of the members of the NATO AVT-240 Task Force on Hypersonic Transition. Victor Sousa also acknowledges the support of the prestigious Lynn Fellowship administered by the interdisciplinary Computational Science and Engineering graduate program at Purdue University.

References

- [1] Reed, H. L., Kimmel, R., Schneider, S., Arnal, D., and Saric, W., "Drag Prediction and Transition in Hypersonic Flow," *AGARD Conference Proceedings*, Vol. 3, AGARD, Neuilly sur Seine, France, 1997, pp. C15–C15.
- [2] DSB, "Report of the Defense Science Board Task Force on the National Aerospace Plane (NASP)," Office of the Under Secretary of Defense for Acquisition, 1988.
- [3] Mack, L., "Boundary-Layer Stability Theory," Document 900-277, Rev. A, Jet Propulsion Lab., Pasadena, CA, 1969.
- [4] Mack, L., "Computation of the Stability of the Laminar Boundary Layer," *Methods in Computational Physics*, Vol. 4, 1965, pp. 247–299.
- [5] Mack, L. M., "On the Inviscid Acoustic-Mode Instability of Supersonic Shear Flows," *Theoretical and Computational Fluid Dynamics*, Vol. 2, No. 2, 1990, pp. 97–123.
- [6] Malmuth, N., Fedorov, A., Shalaev, V., Cole, J., Hites, M., Williams, D., and Khokhlov, A., "Problems in High Speed Flow Prediction Relevant to Control," *2nd AIAA Theoretical Fluid Mechanics Meeting*, AIAA Paper 1998-2695, 1998. doi:10.2514/6.1998-2695
- [7] Fedorov, A. V., Malmuth, N. D., Rasheed, A., and Hornung, H. G., "Stabilization of Hypersonic Boundary Layers by Porous Coatings," *AIAA Journal*, Vol. 39, No. 4, 2001, pp. 605–610. doi:10.2514/2.1382
- [8] Fedorov, A., Shpiilyuk, A., Maslov, A., Burov, E., and Malmuth, N., "Stabilization of a Hypersonic Boundary Layer Using an Ultrasonically Absorptive Coating," *Journal of Fluid Mechanics*, Vol. 479, March 2003, pp. 99–124. doi:10.1017/S0022112002003440
- [9] Fedorov, A. V., Kozlov, V. F., Shpiilyuk, A. N., Maslov, A. A., and Malmuth, N. D., "Stability of Hypersonic Boundary Layer on Porous Wall with Regular Microstructure," *AIAA Journal*, Vol. 44, No. 8, 2006, pp. 1866–1871. doi:10.2514/1.21013
- [10] Chokani, N., Bountin, D. A., Shpiilyuk, A. N., and Maslov, A. A., "Nonlinear Aspects of Hypersonic Boundary-Layer Stability on a Porous Surface," *AIAA Journal*, Vol. 43, No. 1, 2005, pp. 149–155. doi:10.2514/1.9547
- [11] Lukashевич, S., Morozov, S., and Shpiilyuk, A., "Experimental Study of the Effect of a Passive Porous Coating on Disturbances in a Hypersonic Boundary Layer 2. Effect of the Porous Coating Location," *Journal of Applied Mechanics and Technical Physics*, Vol. 57, No. 5, 2016, pp. 873–878. doi:10.1134/S002189441605014X
- [12] Wagner, A., Kuhn, M., Schramm, J. M., and Hannemann, K., "Experiments on Passive Hypersonic Boundary Layer Control Using Ultrasonically Absorptive Carbon–Carbon Material with Random Microstructure," *Experiments in Fluids*, Vol. 54, No. 10, 2013, p. 1606. doi:10.1007/s00348-013-1606-3
- [13] Wagner, A., "Passive Hypersonic Boundary Layer Transition Control Using Ultrasonically Absorptive Carbon–Carbon Ceramic with Random Microstructure," Ph.D. Thesis, Katholieke Univ., Leuven, Belgium, 2014.
- [14] Wagner, A., Hannemann, K., and Kuhn, M., "Ultrasonic Absorption Characteristics of Porous Carbon–Carbon Ceramics with Random Microstructure for Passive Hypersonic Boundary Layer Transition Control," *Experiments in Fluids*, Vol. 55, No. 6, 2014, p. 1750. doi:10.1007/s00348-014-1750-4
- [15] Turner, J., Hoerschgen, M., Jung, W., Stamminger, A., and Turner, P., "SHEFEX—Hypersonic Re-Entry Flight Experiment Vehicle and Subsystem Design, Flight Performance and Prospects," *14th AIAA/AHI Space Planes and Hypersonic Systems and Technologies Conference*, AIAA Paper 2006-8115, 2006. doi:10.2514/6.2006-8115
- [16] Weihs, H., Longo, J., and Turner, J., "The Sharp Edge Flight Experiment SHEFEX II, a Mission Overview and Status," *15th AIAA International Space Planes and Hypersonic Systems and Technologies Conference*, AIAA Paper 2008-2542, 2008.
- [17] Wartemann, V., Wagner, A., Kuhn, M., Eggers, T., and Hannemann, K., "Passive Hypersonic Boundary Layer Transition Control Using an Ultrasonically Absorptive Coating with Random Microstructure: Computational Analysis Based on the Ultrasonic Absorption Properties of Carbon–Carbon," *Procedia IUTAM*, Vol. 14, Jan. 2015, pp. 413–422. doi:10.1016/j.piutam.2015.03.068
- [18] Brès, G., Colonius, T., and Fedorov, A., "Stability of Temporally Evolving Supersonic Boundary Layers over Micro-Cavities for Ultrasonic Absorptive Coatings," *5th AIAA Theoretical Fluid Mechanics Conference*, AIAA Paper 2008-4337, June 2008.
- [19] Fedorov, A., Brès, G., Inkman, M., and Colonius, T., "Instability of Hypersonic Boundary Layer on a Wall with Resonating Micro-Cavities," *49th AIAA Aerospace Sciences Meeting*, AIAA Paper 2011-0373, Jan. 2011.
- [20] Brès, G. A., Inkman, M., Colonius, T., and Fedorov, A. V., "Second-Mode Attenuation and Cancellation by Porous Coatings in a High-Speed Boundary Layer," *Journal of Fluid Mechanics*, Vol. 726, July 2013, pp. 312–337. doi:10.1017/jfm.2013.206
- [21] Egorov, I. V., Fedorov, A. V., and Soudakov, V. G., "Receptivity of a Hypersonic Boundary Layer over a Flat Plate with a Porous Coating," *Journal of Fluid Mechanics*, Vol. 601, 2008, pp. 165–187. doi:10.1017/S0022112008000669
- [22] De Tullio, N., and Sandham, N. D., "Direct Numerical Simulation of Breakdown to Turbulence in a Mach 6 Boundary Layer over a Porous Surface," *Physics of Fluids*, Vol. 22, No. 9, 2010, p. 094105. doi:10.1063/1.3481147
- [23] Wang, X., and Zhong, X., "Effect of Porous Coating on Boundary-Layer Instability," *48th AIAA Aerospace Sciences Meeting*, AIAA Paper 2010-1243, Jan. 2010.
- [24] Scalò, C., Bodart, J., and Lele, S. K., "Compressible Turbulent Channel Flow with Impedance Boundary Conditions," *Physics of Fluids*, Vol. 27, No. 3, 2015, Paper 035107.
- [25] Taylor, G. I., and Maccoll, J., "The Air Pressure on a Cone Moving at High Speeds. 1," *Proceedings of Royal Society of London A*, Vol. 139, No. 838, 1933, pp. 278–297.
- [26] Mangler, W., "Zusammenhang Zwischen Ebenen und Rotations-symmetrischen Grenzschichten in Kompressiblen Flüssigkeiten," *ZAMM—Journal of Applied Mathematics and Mechanics/Zeitschrift für Angewandte Mathematik und Mechanik*, Vol. 28, No. 4, 1948, pp. 97–103. doi:10.1002/(ISSN)1521-4001
- [27] Illingworth, C., "Steady Flow in the Laminar Boundary Layer of a Gas," *Proceedings of Royal Society of London A*, Vol. 199, Dec. 1949, pp. 533–558.
- [28] Lees, L., "Laminar Heat Transfer over Blunt-Nosed Bodies at Hypersonic Flight Speeds," *Journal of Jet Propulsion*, Vol. 26, No. 4, 1956, pp. 259–269. doi:10.2514/8.6977
- [29] Cook, A. W., "Artificial Fluid Properties for Large-Eddy Simulation of Compressible Turbulent Mixing," *Physics of fluids*, Vol. 19, No. 5, 2007, p. 055103. doi:10.1063/1.2728937
- [30] Kawai, S., and Lele, S. K., "Localized Artificial Diffusivity Scheme for Discontinuity Capturing on Curvilinear Meshes," *Journal of Computational Physics*, Vol. 227, No. 22, 2008, pp. 9498–9526. doi:10.1016/j.jcp.2008.06.034
- [31] Lele, S. K., "Compact Finite Difference Schemes with Spectral-Like Resolution," *Journal of Computational Physics*, Vol. 103, No. 1, 1992, pp. 16–42. doi:10.1016/0021-9991(92)90324-R
- [32] Jiang, X., and Lai, C.-H., *Numerical Techniques for Direct and Large-Eddy Simulations*, CRC Press, 2009.
- [33] Nagarajan, S., Lele, S. K., and Ferziger, J. H., "A Robust High-Order Compact Method for Large Eddy Simulation," *Journal of Computational Physics*, Vol. 191, No. 2, 2003, pp. 392–419. doi:10.1016/S0021-9991(03)00322-X

- [34] Nagarajan, S., Lele, S., and Ferziger, J., "Leading-Edge Effects in Bypass Transition," *Journal of Fluid Mechanics*, Vol. 572, 2007, pp. 471–504.
doi:10.1017/S0022112006001893
- [35] Fung, K.-Y., and Ju, H., "Time-Domain Impedance Boundary Conditions for Computational Acoustics and Aeroacoustics," *International Journal of Computational Fluid Dynamics*, Vol. 18, No. 6, 2004, pp. 503–511.
doi:10.1080/10618560410001673515
- [36] Poinso, T. J., and Lele, S. K., "Boundary Conditions for Direct Simulations of Compressible Viscous Flows," *Journal of Computational Physics*, Vol. 101, No. 1, 1992, pp. 104–129.
doi:10.1016/0021-9991(92)90046-2
- [37] Patel, D., Gupta, P., and Scalo, C., "Surface Impedance Determination via Numerical Resolution of the Inverse Helmholtz Problem," *23rd AIAA/CEAS Aeroacoustics Conference*, AIAA Paper 2017-3695, 2017.
doi:10.2514/6.2017-3695
- [38] Patel, D., Gupta, P., Scalo, C., Rothermel, T., and Kuhn, Markus, "Towards Impedance Characterization of Carbon-Carbon Ultrasonically Absorptive Coatings via the Inverse Helmholtz Problem," *55th AIAA Aerospace Sciences Meeting*, AIAA Paper 2017-0460, 2017.
- [39] Wagner, A., Martinez Schramm, J., Dittert, C., Sousa, V., Patel, D. I., and Scalo, C., "Experimental and Numerical Acoustic Characterization of Ultrasonically Absorptive Porous Materials," *2018 Joint Thermophysics and Heat Transfer Conference*, AIAA Paper 2018-2948, 2018.
- [40] Lin, J., Scalo, C., and Hesselink, L., "High-Fidelity Simulation of a Standing-Wave Thermoacoustic-Piezoelectric Engine," *Journal of Fluid Mechanics*, Vol. 808, 2016, pp. 19–60.
doi:10.1017/jfm.2016.609
- [41] Möser, M., *Engineering Acoustics: an Introduction to Noise Control*, Springer Science and Business Media, 2009.
- [42] Fedorov, A. V., Malmuth, N. D., Rasheed, A., and Hornung, H. G., "Stabilization of Hypersonic Boundary Layers by Porous Coatings," *AIAA Journal*, Vol. 39, No. 4, 2001, pp. 605–610.
doi:10.2514/2.1382
- [43] Johnson, D. L., Koplik, J., and Dashen, R., "Theory of Dynamic Permeability and Tortuosity in Fluid-Saturated Porous Media," *Journal of Fluid Mechanics*, Vol. 176, March 1987, pp. 379–402.
doi:10.1017/S0022112087000727
- [44] Allard, J.-F., and Champoux, Y., "New Empirical Equations for Sound Propagation in Rigid Frame Fibrous Materials," *Journal of the Acoustical Society of America*, Vol. 91, No. 6, 1992, pp. 3346–3353.
doi:10.1121/1.402824
- [45] Gaster, M., and Grant, I., "An Experimental Investigation of the Formation and Development of a Wave Packet in a Laminar Boundary Layer," *Proceedings of the Royal Society of London A: Mathematical, Physical and Engineering Sciences*, Vol. 347, 1975, pp. 253–269.
- [46] Sivasubramanian, J., and Fasel, H. F., "Numerical Investigation of the Development of Three-Dimensional Wavepackets in a Sharp Cone Boundary Layer at Mach 6," *Journal Fluid Mechanics*, Vol. 756, Oct. 2014, pp. 600–649.
doi:10.1017/jfm.2014.434
- [47] Stetson, K. F., "Comments on Hypersonic Boundary-Layer Transition," Tech. Rept., Wright Research and Development Center, Wright Patterson Air Force Base, 1990.
- [48] Fedorov, A. V., "Receptivity of a High-Speed Boundary Layer to Acoustic Disturbances," *Journal of Fluid Mechanics*, Vol. 491, 2003, pp. 101–129.
doi:10.1017/S0022112003005263
- [49] Dittert, C., and Kütemeyer, M., "Octra-Optimized Ceramic for Hypersonic Application with Transpiration Cooling," *Advances in High Temperature Ceramic Matrix Composites and Materials for Sustainable Development*, Vol. 263, June 2017, p. 389.
- [50] Wagner, A., Wärtemann, V., Kuhn, M., Dittert, C., and Hannemann, K., "The Potential of Ultrasonically Absorptive TPS Materials for Hypersonic Vehicles," *20th AIAA International Space Planes and Hypersonic Systems and Technologies Conference*, AIAA Paper 2015-3576, 2015.
- [51] Fella, Z. E. A., Berger, S., Lauriks, W., Depollier, C., Aristegui, C., and Chapelon, J.-Y., "Measuring the Porosity and the Tortuosity of Porous Materials via Reflected Waves at Oblique Incidence," *Journal of the Acoustical Society of America*, Vol. 113, No. 5, 2003, pp. 2424–2433.
doi:10.1121/1.1567275
- [52] Willems, S., Gülhan, A., Ward, C. A., and Schneider, S. P., "Free Transition on a Slender Cone in a Quiet and a Conventional Wind Tunnel and the Effect of Ultrasonically Absorptive Materials," *Progress in Flight Physics*, Vol. 9, 2017, pp. 497–516.

R. M. Cummings
Associate Editor